

Features of the Energy Balance and Fragmentation Mechanisms at Spontaneous Failure of Class I and Class II Rocks

Boris G. Tarasov¹ · Thomas R. Stacey²

Received: 4 April 2017 / Accepted: 25 May 2017 / Published online: 6 June 2017
© Springer-Verlag Wien 2017

Abstract Practically, all types of rockbursts are accompanied by release of seismic energy, rock bulking (due to fracturing and fragmentation), and ejection of fragmented rocks in the opening. Principles of the energy redistribution during rockbursts in some regards are comparable with principles taking place at spontaneous failure of rock specimens under compression in loading systems. In both cases, the total potential elastic energy accumulated in the failing material and in the loading system (or surrounding rock mass) is converted into such components of dynamic energy as rupture energy, seismic energy (or energy of oscillation of the loading system due to dynamic energy release), and kinetic energy of flying fragments of the failed material. It is known that spontaneous failure takes place at the post-peak failure stage and is determined by the ratio between stiffness of the loading system and stiffness (or brittleness) of the failing material. However, principles of the energy redistribution between different components of the energy balance are still unclear. The paper discusses results of laboratory experiments conducted on rock specimens of different brittleness (including Class I and Class II) that were loaded in testing machines of different loading stiffness. The most brittle of the tested

specimens are represented by quartzite and glass, and the less brittle by salt. The loading stiffness of testing machines used in experiments was variable within three decimal orders of magnitude. The specific variations of the dynamic energy balance depending on rock brittleness and loading stiffness were established. The role of each portion of elastic energy stemming from the specimen and from the loading system in determining the dynamic energy balance and fragmentation mechanisms operating at spontaneous failure is analysed. The results obtained contribute to the understanding of dynamic processes taking place during rockbursts.

Keywords Spontaneous rock failure · Dynamic energy balance · Fragmentation mechanism · Material brittleness · Class I and Class II failure mode

List of symbols

E	Elastic modulus
M	Post-peak modulus
σ	Axial stress
ε	Axial strain
F	Axial force
d	Axial displacement
W_e	Elastic energy stored in the specimen at the peak stress
W_r	Total post-peak rupture energy
$W_{r.in}$	Internal component of static post-peak rupture energy
$W_{r.ex}$	External component of static post-peak rupture energy
$\Delta W_{r(d)}$	Dynamic increment of the post-peak rupture energy
W_d	Surplus elastic energy responsible for dynamics
W_k	Kinetic energy of rock fragments

✉ Boris G. Tarasov
boris.tarasov@uwa.edu.au
Thomas R. Stacey
Thomas.Stacey@wits.ac.za

¹ Centre for Offshore Foundation Systems, The University of Western Australia, 35 Stirling Highway, Crawley, WA 6009, Australia

² School of Mining Engineering, University of the Witwatersrand, Private Bag 3, Johannesburg 2050, South Africa

W_{se}	Seismic energy
dW_e	Total elastic energy withdrawn from the specimen during post-peak failure
dW_a	Elastic energy released during spontaneous failure
m_o	Inertial mass of the specimen
m_H	Inertial mass of the loading system
K_1	Brittleness index

1 Introduction

Understanding the rockburst damage mechanism is critical to implement rockburst support for elimination and mitigation of rockburst hazard. Ortlepp and Stacey (1994) classified rockbursts into five types (strainburst, buckling, face crush/pillar burst, shear rupture, and fault-slip burst). Practically, all types of rockbursts are accompanied by release of seismic energy, rock bulking (due to fracturing and fragmentation of previously intact or less fractured media), and ejection of fragmented rocks into the opening. Ejected rock may travel at velocities in excess of 3 m/s; McGarr (1997) referred to "... numerous observations, in nearby damaged tunnels... imply wall-rock velocities of the order of 10 m/s and greater". Observations from rockburst damage indicate large variations in parameters such as failure violence, degree of rock fragmentation, volume of ejected rock, ejection velocity. These manifestations of rockbursts are related to the potential elastic energy stored in the rock during loading and how this stored energy is released during spontaneous failure (dynamic energy balance).

To cause one of the first three types of burst, the rock mass surrounding the fracturing rock adjoining the opening must create a relatively "soft" loading environment such that the rock fails in an unstable and violent manner (Cook 1965; Ortlepp and Stacey 1994; Kaiser and Cai 2013). It is known that the macroscopic spontaneous failure takes place at the post-peak failure stage, which implies that post-peak properties of the failing rock play a paramount role in the stability determination. For example, in Class I mode of rock failure (characterised by a negative post-peak modulus $M = d\sigma/d\varepsilon < 0$ in Wawersik and Fairhurst (1970)), it is possible to prevent dynamic events by increasing stiffness of the loading environment above the post-peak stiffness. However, in Class II mode of rock failure (characterised by a positive post-peak modulus $M = d\sigma/d\varepsilon > 0$), the instability condition is satisfied even for an absolutely stiff loading environment, providing for unavoidable spontaneous failure. Two other types of rockbursts (shear rupture and fault-slip burst) nucleated some distance away from the opening under conditions of triaxial compression can be also associated with both Class I and Class II rock behaviour.

Principles of the energy redistribution during rockbursts, in some regards, are comparable with principles involved in spontaneous failure of rock specimens in compression in loading systems. From the point of view of stability determination, Class I and Class II modes of rock failure are critically different. We can also expect a significant difference in fragmentation mechanisms associated with these two classes of rock behaviour. This question is still insufficiently studied, as is the role of the two components of elastic energy, stemming from the failing rock and from the loading system, in determining rock fracturing, fragmentation, failure violence, and ejection velocity.

One of the reasons for insufficient experimental studies of these questions is the suggestion that the post-peak behaviour is not an essential property of the material and cannot be represented as constitutive behaviour (Clucklich and Cohen 1967; Drescher and Vardoulakis 1982; Read and Hegemier 1984; Labuz and Biolzi 1991). Indeed, experiments show that the same softening material can appear with Class I as well as Class II stability behaviour depending on the specimen size and geometry (Read and Hegemier 1984; Labuz and Biolzi 1991). At the same time, if, in experiments, we use specimens of the same size and geometry made from different materials, we can observe a specific and reproducible behaviour of each material in the post-peak region. For example, one material can always demonstrate Class I behaviour, while another material demonstrates Class II behaviour. Furthermore, it is known that increasing confining pressure makes some rocks more ductile in post-peak failure, while other rocks exhibit dramatic embrittlement, changing from Class I to extreme Class II behaviour (e.g. Tarasov 2010). All this indicates that post-peak response is a reflection of some intrinsic material properties. The use of the same size and geometry of specimens in experiments allows relative post-peak properties of different materials and their influence on the dynamic energy balance at spontaneous failure to be estimated.

It should be noted that post-peak failure has been mainly studied at controllable and constant strain rate regimes (Wawersik and Fairhurst 1970; Bieniawski 1970; Hudson et al. 1972; Okubo et al. 1990; Lockner et al. 1992; Dight et al. 2013; Xu and Cai 2017). The study of the energy balance at spontaneous failure, with experimental determination of such energy components as dynamic rupture energy, kinetic energy of flying fragments, and seismic energy, has been described in detail in Stavrogin and Tarasov (2001). The current paper proposes some additional analysis of the laboratory results from this work and also presents some new results. It shows specific variations of the dynamic energy balance depending on rock brittleness and loading stiffness. The role of each portion of elastic energy, stemming from the specimen and from the

loading system in determining the dynamic energy balance and fragmentation mechanisms operating at spontaneous failure, is analysed. The following two types of fragmentation mechanisms are considered: compressive-force mechanism caused by external forces affecting the failing material and failure wave mechanism caused by shock waves generated by dynamic release of external forces. Experimental results analysed in the paper were obtained at testing of about a hundred specimens of the same geometry and size: cylindrical specimens with diameter about 30–35 mm and length about 60–70 mm.

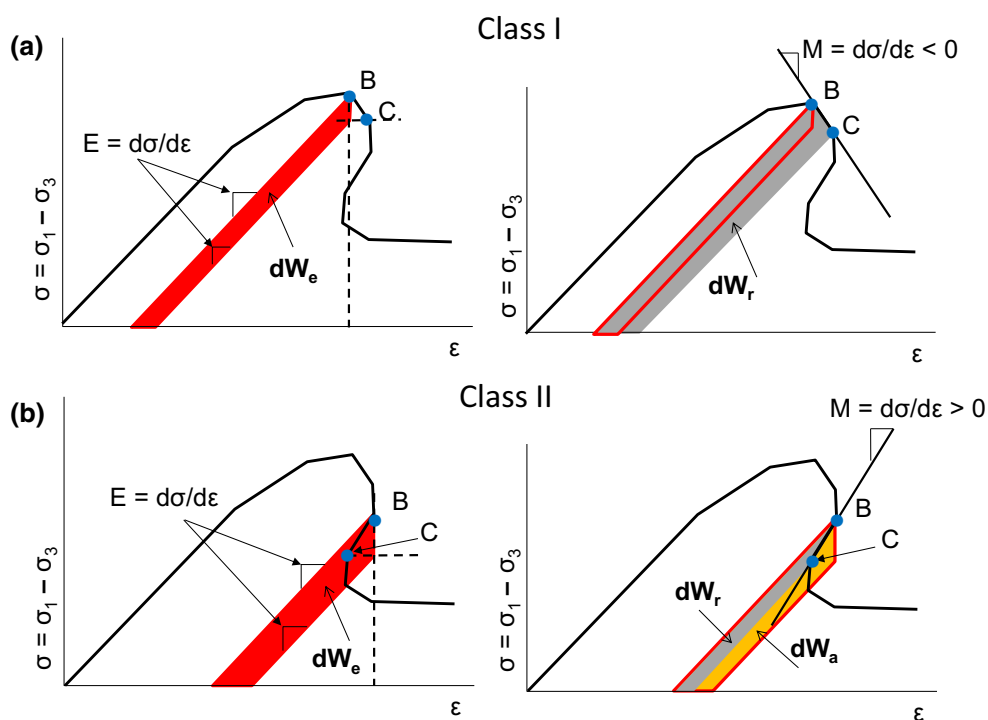
2 Intrinsic Rock Brittleness at Compression

Conditions of stable or unstable (spontaneous) post-peak failure in laboratory experiments are determined by the relation between post-peak specimen stiffness and loading stiffness. In the spontaneous regime, the degree of failure violence is determined by the relation between elastic energy stored in the system ‘specimen-loading machine’ and post-peak rupture energy. It is accepted that competition between elastic energy stored in the specimen and dissipated fracture energy characterises the material brittleness (Labuz and Biolzi 1991). There are different brittleness indexes reflecting this competition, which can be used for characterisation of material brittleness (Coates 1966; Hucka and Das 1974; Kidybinski 1981; Bergman

and Stille 1983; Petoukhov and Linkov 1983; Stavrogin and Protossenia 1985; He et al. 1990; Aubertin et al. 1994; Andreev 1995). An important advantage of the brittleness index K_1 used in this paper is the fact that, unlike other existing criteria, it allows the monotonic variation of the material brittleness from absolute brittleness (failure without energy consumption) to absolute ductility to be represented as a function of monotonic variation of post-peak modulus $M = d\sigma/d\varepsilon$ from extreme Class II ($M = E$) to extreme Class I ($M = 0$) (Tarasov 2010; Tarasov and Potvin 2013). Such representation of material brittleness forms a universal scale of brittleness. It is because, in experiments discussed in this paper, we use specimens of the same geometry and size the index K_1 and the universal scale of brittleness will allow the relative brittleness of the tested rocks to be estimated. Brief information about index K_1 and the universal scale of brittleness is represented in this section.

Characteristics of intrinsic material properties, before and after the peak stress is reached, can be obtained from the complete stress–strain (or load–displacement) curves. The post-peak curve in Fig. 1 at different stages corresponds to Class I (Fig. 1a) and Class II (Fig. 1b) behaviour. Points B and C for both stages represent points located infinitely near to each other on the post-peak curve. The failure process between points B and C can be characterised by the following types of specific (per unit volume) energy:

Fig. 1 Principle of determination of brittleness index K_1



- Elastic energy withdrawn from the specimen (red area, or delineated by the red line)

$$dW_e = \frac{\sigma_B^2 - \sigma_C^2}{2E}, \tag{1}$$

- Rupture energy absorbed by the specimen (grey area)

$$dW_r = \frac{(\sigma_B^2 - \sigma_C^2)(M - E)}{2EM}, \tag{2}$$

- Released energy (yellow area representing the excess of elastic energy which was not absorbed by the rupture process)

$$dW_a = \frac{\sigma_B^2 - \sigma_C^2}{2M}. \tag{3}$$

The brittleness index K_1 is determined by the ratio between the rupture energy and the withdrawn elastic energy:

$$K_1 = \frac{dW_r}{dW_e} = \frac{M - E}{M}. \tag{4}$$

This index characterises the capability of the rock for self-sustaining failure due to the elastic energy available from the material. In other words, it characterises the degree of intrinsic instability of the material at failure. It is important to note that K_1 characterises the intrinsic rock brittleness independently of the loading stiffness.

Figure 2 shows the universal scale of brittleness based upon the index K_1 , with brittleness increasing from left to right. The complete stress–strain curves illustrate how the different shapes of post-peak curves (indicated by dotted blue lines with different post-peak modulus M) describe a

variation in brittleness. Elastic modulus E for all curves is considered the same. Areas delineated by red lines correspond with elastic energy W_e stored in the specimen at the peak stress and withdrawn during the post-peak failure process. Grey areas represent the post-peak rupture energy W_r at complete failure. Yellow areas correspond with the released energy. The important point on the scale is $K_1 = 1$ representing the intermediate situation between Class I and Class II behaviour. On the right of this point, the material behaviour is Class II, characterised as self-sustaining failure. The closer the value of K_1 is to zero, the more brittle the material and the more violent the failure. At absolute brittleness, $K_1 = 0$, $E = M$, and the post-peak rupture energy is equal to zero ($W_r = 0$), which means that the total elastic energy stored in the material body will be transformed into seismic energy and kinetic energy of flying fragments. On the left of the point $K_1 = 1$, self-sustaining failure is impossible, and some additional energy from the loading system is necessary to cause the post-peak failure development. The greater the brittleness index K_1 in this region, the more ductile the post-peak rock behaviour. The index K_1 and the universal scale of brittleness are based on sound physics principles and thus provide proper characterisation of rock brittleness for all types of rock and testing conditions (unconfined and confined compression).

3 Controllable and Spontaneous Post-peak Failure

3.1 General Approach

Figure 3a shows a pre-peak force–displacement curve OB for a tested specimen and a characteristic of the loading stiffness BR , with corresponding portions of elastic energy

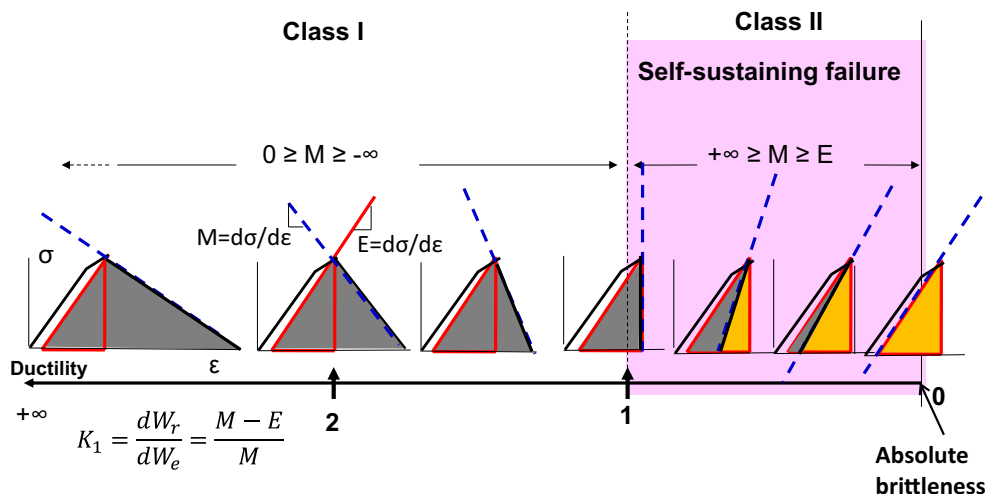


Fig. 2 Universal scale of rock brittleness at compression

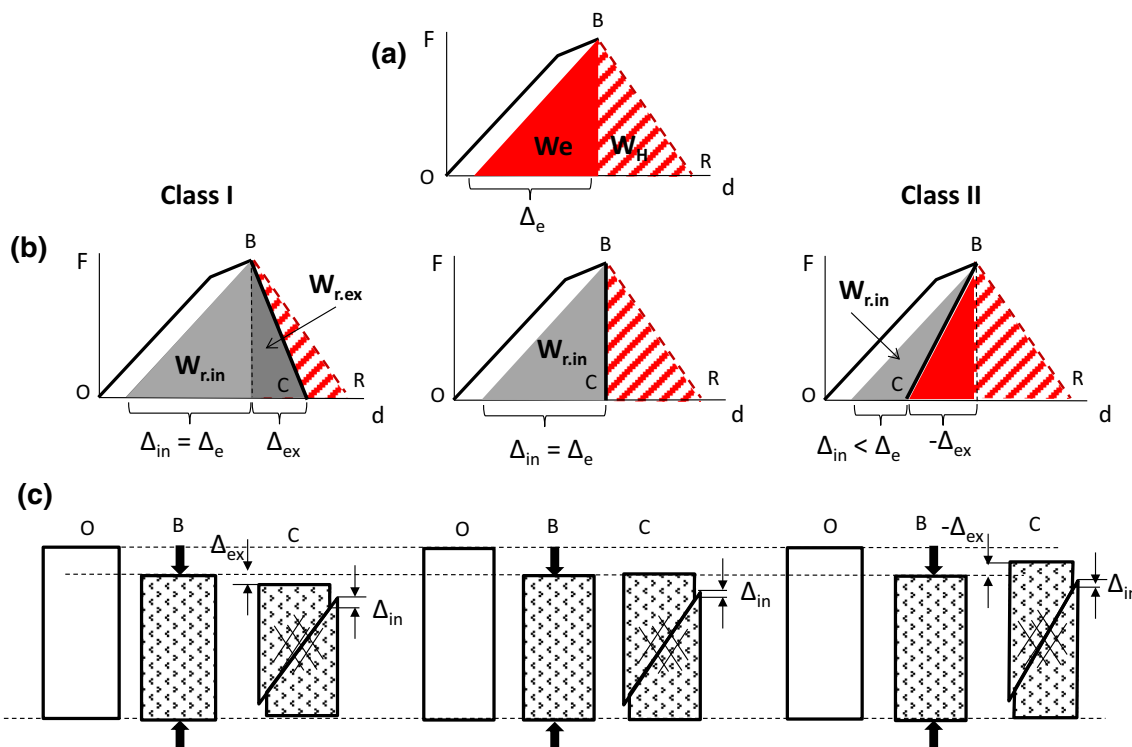


Fig. 3 Post-peak energy balance of servo-controlled failure for Class I, Class II, and intermediate rocks

W_e and W_H stored in the specimen and the loading system at point B, which represents the peak load. We will refer to the elastic energy W_e as internal energy and the elastic energy W_H as external energy. Figure 3b shows three complete force–displacement curves OBC representing Class I, Class II, and intermediate rock behaviour. The post-peak curves BC and post-peak rupture energy W_r (grey areas) here represent rock properties at static controllable failure. For all cases, the total amount of elastic energy stored at the peak load exceeds the post-peak rupture energy ($W_e + W_H > W_r$). The spontaneous failure in such a situation can be prevented through extraction of the excessive elastic energy during the failure process by a servo-control system.

Figure 3c shows features of the deformation process in the static controllable regime for all three cases. At stages O, B, and C the specimen is, respectively, before loading, at the peak load, and at complete failure. Failure mechanisms operating in the post-peak region are normally associated with different combinations of such processes as distributed cracking and localised shear rupture development. For the intermediate situation during the post-peak failure from point B to point C, the external deformation between the specimen ends is equal to zero ($\Delta_{ex} = 0$). The post-peak rupture energy in this case is associated with the internal irreversible deformation Δ_{in} caused by the elastic energy stemming from the specimen, W_e . The post-peak

rupture energy produced by the internal elastic energy, W_e , is referred to as the internal post-peak rupture energy, $W_{r.in}$. For Class I, the total post-peak rupture energy includes two portions: internal post-peak rupture energy $W_{r.in}$ and external post-peak rupture energy $W_{r.ex}$ associated with the external irreversible deformation Δ_{ex} produced by the loading system. For Class II, the external deformation is associated with reversal of elastic unloading of the specimen ($-\Delta_{ex}$), which is accompanied by extraction of the excess elastic energy. This external deformation is elastic, and consequently, it is not associated with the rupture process. The rest of the internal elastic energy stemming from the specimen creates the post-peak internal irreversible deformation Δ_{in} and transforms into the post-peak rupture energy $W_{r.in}$.

Without servo-control, the failure process in all three cases should be spontaneous, because, at any stage of failure, the portion of elastic energy withdrawn from the specimen and loading system exceeds the portion of rupture energy absorbed by the rupture process, that is, $dW_e + dW_H > dW_r$. High deformation rate at spontaneous (dynamic) failure should affect the post-peak rupture energy. The surplus of elastic energy will be distributed between different types of dynamic energy. Principles of the energy redistribution during spontaneous failure will be analysed later in the paper on the basis of experimental results obtained on Class I and Class II rocks.

3.2 Testing Method

Figure 4 shows schematically the testing machine used in experiments on Class I and Class II rocks. Loading principles involved in this machine are described in Stavrogin and Tarasov (2001). The machine consists of a stiff monolithic frame, a stiff loading actuator, and a servo-controlled system. In this version, the loading stiffness is 20 MN/mm, which provides controllable static post-peak failure of brittle rocks. To vary the loading stiffness, different replaceable elastic elements (shown as a spring in the schematic) were installed between the actuator and the specimen. The elastic elements serve as accumulators of elastic energy within the loading system during the specimen loading. Due to the extremely high stiffness of the main loading system, the amount of elastic energy stored in it is negligibly small compared with the elastic energy stored in the elastic element. These elements, made from hardened spring steel in the form of hollow cylinders or rings with different wall thickness, provide a large range of loading stiffness (more than three decimal orders of magnitude). Thus, stiffness of the loading system can be varied within the range between 20 MN/mm and about 20 KN/mm. To the upper end of the elastic element a replaceable inertial mass is attached.

To study the role of the loading stiffness in the energy balance during post-peak failure, a series of at least four identical specimens of the same rock was tested at different regimes. The first specimen was tested at static controllable regime to determine the specimen stiffness. The rest

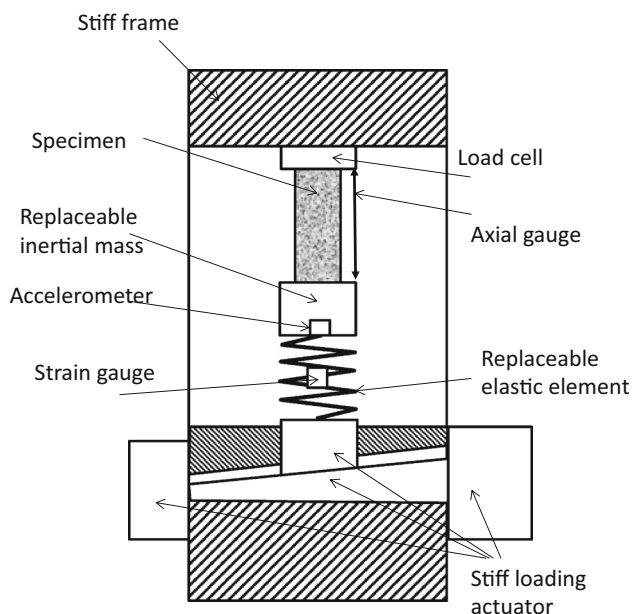


Fig. 4 Testing machine for the study of the energy balance during spontaneous failure at different levels of loading stiffness

specimens were tested at spontaneous regimes where the rate between the loading stiffness S_l and specimen stiffness S_s varied with approximately the following steps: $S_l/S_s \approx 0.7$; 0.5; 0.3; 0.2; 0.1. The variation of the energy balance with variation of the loading stiffness for eight different rocks testing on this machine is discussed in Sect. 4.2.

Experiments under the spontaneous regime were conducted as follows: a specimen was placed on an inertial mass and loaded statically up to the peak stress, beyond which the specimen failed dynamically due to the elastic energy accumulated within the loading system and the specimen. During each test, the data were recorded by a set of gauges, including a load cell, strain gauges attached to the specimen and to the elastic element, and also by a piezoelectric accelerometer fixed to the inertial mass. The data were recorded both during the static loading before the peak stress and during spontaneous dynamic failure in the post-peak region. The main idea of the experiments conducted was to investigate how the elastic energy accumulated in the specimen body and in the loading system transforms into other forms of energy during spontaneous failure.

4 Energy Balance for Class I Rocks at Spontaneous Failure and Compressive-Force Fragmentation Mechanism

4.1 Conditions of Spontaneous Failure

The schematic representation of different stages of the spontaneous failure process in Fig. 5 simplifies explanation of experimental results. The loading system in Fig. 5a is shown as a spring with the attached inertial mass (i.m.). Stage (I) here corresponds to the peak stress in Fig. 5b. Portions of elastic energy stored in the specimen W_e and in the loading system W_H at the peak stress are shown by red triangles. Figure 5c explains the energy balance at spontaneous failure. The dotted line BC represents the static post-peak curve corresponding to the controllable regime. Portions of internal and external post-peak rupture energy $W_{r.in}$ and $W_{r.ex}$ of the static failure are represented by corresponding grey triangular areas. It is known that increasing deformation rate (or strain rate) in the post-peak region changes the post-peak rock properties (e.g. Bieniawski 1970; Okubo et al. 1990; Stavrogin and Tarasov 2001). The post-peak rupture energy at spontaneous dynamic failure can be changed by $\Delta W_{r(d)}$, represented by the hatched grey triangular area. This portion of energy is referred to as a dynamic increment of the post-peak rupture energy. The line BC' represents the dynamic post-peak curve obtained at spontaneous failure.

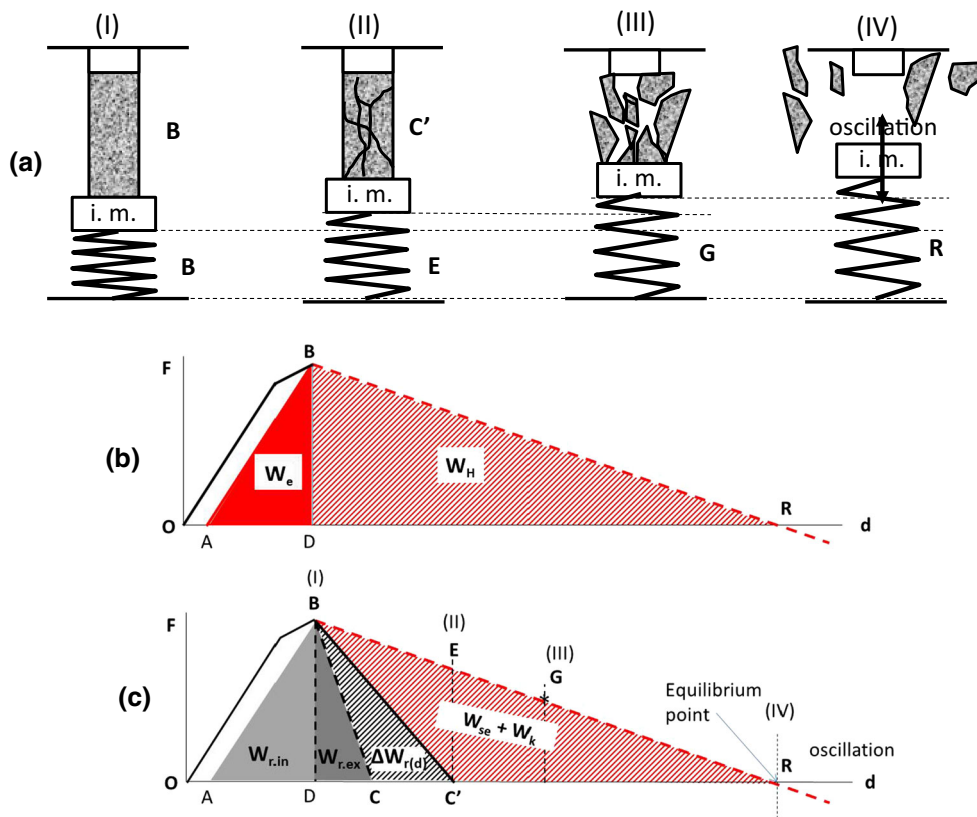


Fig. 5 Different stages of the spontaneous failure process caused by soft loading system for Class I rocks

It is important to note that, during spontaneous failure, the deformation compatibility condition between the loading system and the specimen is satisfied, implying permanent contact between the specimen ends and the loading system. At the same time, the potential force capacity of the loading system (BE in Fig. 5c) exceeds the bearing capacity of the failing specimen (BC'). At stage II, specimen failure has completed. At this moment, the bearing capacity of the specimen becomes equal (or close) to zero, corresponding to point C'. However, the force capacity of the loading system is high, corresponding to point E. The surplus of elastic energy BC'E, stemming from the loading system during the specimen failure, is responsible for dynamics and acceleration of the failure process. After stage II, the spring element (loading system) with the attached inertial mass (i.m.) and the specimen fragments located on it continues moving. Initially, it moves with acceleration which speeds up the specimen fragments. The loading system at this stage acts as a catapult. At a certain stage of movement (stage III corresponding to point G), the loading system reaches the maximum speed, providing the same speed to the rock fragments, and then it decelerates, separating from the rock fragments, and is finally in an oscillation mode.

In each test, the gauges shown in Fig. 4 allowed determination of the following parameters. On the basis of

the complete load–displacement curves, recorded by the load cell and axial gauge (in controllable and spontaneous post-peak regimes), the following components of the energy balance were determined: the elastic energy W_e stored in the specimen at the peak stress (or at the moment of start of instability); the internal $W_{r,in}$ and external $W_{r,ex}$ components of static post-peak rupture energy; and the dynamic increment of the post-peak rupture energy $\Delta W_{r(d)}$. The strain gauge fixed to the elastic element, in combination with the load cell, provided the information about the loading stiffness and the elastic energy W_H accumulated in the loading system at the peak stress. The specially calibrated accelerometer (see details in Stavrogin and Tarasov 2001) attached to the inertial mass allowed determination of the seismic energy W_{se} associated with oscillation of the loading system after rock failure. A portion of energy transmitted into kinetic energy W_k of rock fragments accelerated by the loading system after specimen failure was calculated on the basis of Eq. (5), determined experimentally in Stavrogin and Tarasov (2001):

$$W_k = W_{se} \frac{m_o}{m_H} \tag{5}$$

Here, m_H is the inertial mass of the loading system; m_o is the inertial mass of the specimen.

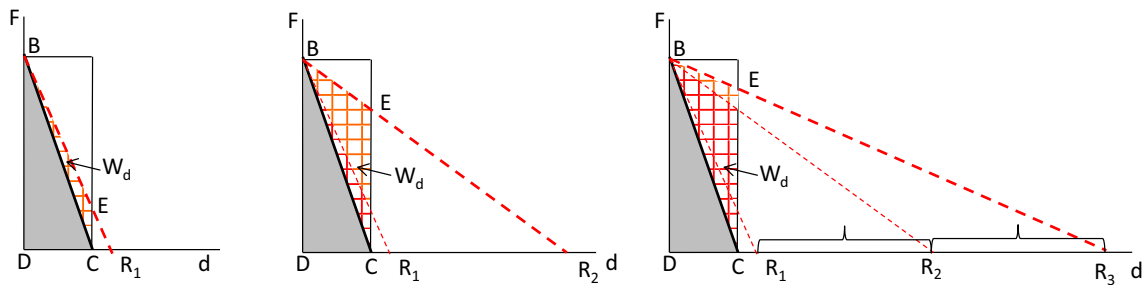
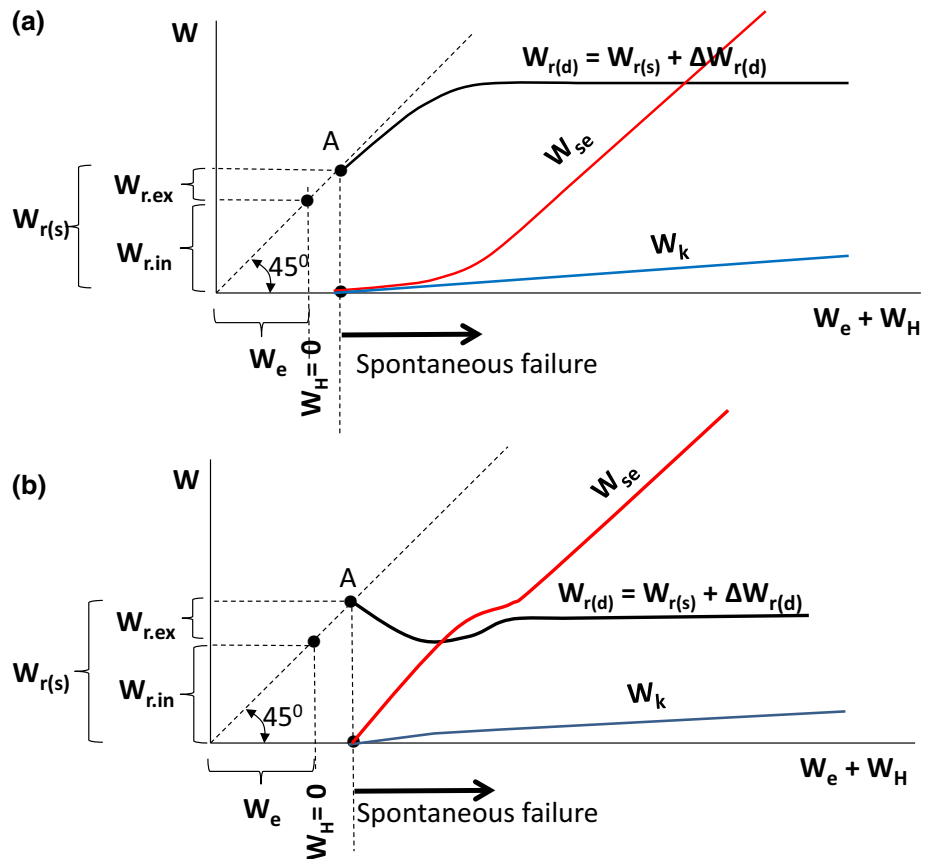


Fig. 7 Explanation for the restricted effect of the loading stiffness on the post-peak rupture energy

Fig. 8 Schematic representation of the total energy balance versus elastic energy stored in the specimen and loading system ($W_e + W_H$) for Class I rocks



Schematic representation of the total energy balance, including internal elastic energy W_e and internal post-peak rupture energy $W_{r.in}$ for both groups of rocks, is shown in Fig. 8. The horizontal axis represents the elastic energy stored in the specimen, W_e , and in the loading system, W_H . The vertical axis characterises values of the different types of energy into which the elastic energy transforms at failure. Figure 8a represents rocks of group (a), while Fig. 8b represents rocks of group (b). Spontaneous failure takes place when the total elastic energy ($W_e + W_H$) exceeds the static post-peak rupture energy $W_{r(s)} = W_{r.in} + W_{r.ex}$. The graphs demonstrate that, in the static and dynamic regimes, elastic energy W_e stemming from the specimen is totally transformed into internal post-peak rupture energy $W_{r.in}$.

Changes in the energy components at spontaneous failure are provided solely by the elastic energy W_H stemming from the loading system. The energy W_H transforms into the post-peak rupture energy increment $\Delta W_{r(d)}$, seismic energy W_{se} , and kinetic energy of rock fragments W_{fr} . At low loading stiffness, when the dynamic post-peak rupture energy $W_{r(d)} = W_{r(s)} + \Delta W_{r(d)}$ becomes constant, the majority of the elastic energy stemming from the loading system transforms into the seismic energy W_{se} .

It should again be noted that, in the experiments discussed, the specimens were loaded (or deformed) statically up to the moment of spontaneous failure in the post-peak region. All rocks used in these experiments were tested also in the ‘common’ dynamic regime, with constant strain rate

before and after peak stress (see stress–strain curves in “Appendix”). These experiments showed that rock behaviour under ‘common’ dynamics was similar to that observed at spontaneous failure: rocks of group (a) increased post-peak rupture energy in dynamic conditions, becoming more ductile, while rocks of group (b) decreased post-peak rupture energy in dynamic conditions, becoming more brittle.

Results presented in Fig. 6 show that for all tested rocks of different brittleness, the rate $\Delta W_{r(d)}/W_{r,ex}$ does not exceed 3. If we suppose that the rate $\Delta W_{r(d)}/W_{r,ex} = 3$ represents a maximum for all Class I rocks, we can estimate how the post-peak rupture energy can be changed at spontaneous failure for rocks of different brittleness characterised by K_1 . Figure 9a illustrates the idea. It shows complete static force–displacement curves ABC for different $K_1 = W_r/W_e = (W_{r,in} + W_{r,ex})/W_e$. Here, for example, the curve for $K_1 = 3$ corresponds to marble, the curve for $K_1 = 1.5$ corresponds to sulphide ore, and the curve for $K_1 = 1.1$ corresponds to sandstone-1 and sandstone-2. Lines BC' on the graphs represent dynamic post-peak curves for the situation when

$$\frac{\Delta W_{r(d)}}{W_{r,ex}} = 3. \tag{6}$$

The dynamic increment of the post-peak rupture energy $\Delta W_{r(d)}$ is shown on the graphs by hatched triangles. Graphs

in Fig. 9a demonstrate that the closer the value of K_1 is to unity, the smaller is the absolute value of $\Delta W_{r(d)}$, approaching zero at $K_1 = 1$. If we express the brittleness index K_1 as follows:

$$K_1 = \frac{W_{r,in} + W_{r,ex}}{W_e} = \frac{W_{r,in} + W_{r,ex}}{W_{r,in}} = 1 + \frac{W_{r,ex}}{W_{r,in}},$$

we will have:

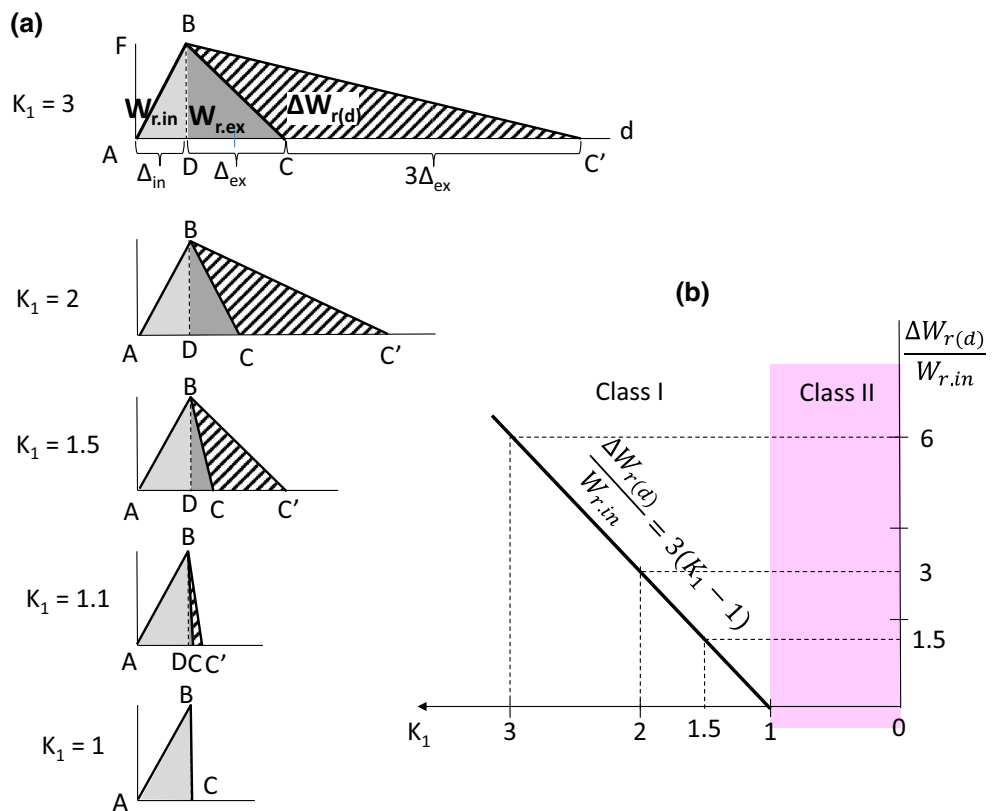
$$W_{r,ex} = (K_1 - 1)W_{r,in}. \tag{7}$$

Using Eqs. (6) and (7) we can determine the rate $\Delta W_{r(d)}/W_{r,in}$ which characterises the relative dynamic increment of the post-peak rupture energy caused by spontaneous failure depending on rock brittleness index K_1 :

$$\frac{\Delta W_{r(d)}}{W_{r,in}} = 3(K_1 - 1). \tag{8}$$

The meaning of Eq. (8) is illustrated graphically in Fig. 9b. It shows that for Class I rocks the relative dynamic increment of post-peak rupture energy $\Delta W_{r(d)}$ decreases with increasing rock brittleness and approaches zero at $K_1 = 1$. The fact that at $K_1 = 1$ the increment $\Delta W_{r(d)} = 0$ indicates that the internal rupture energy $W_{r,in}$ stays the same at static and at dynamic spontaneous failure. It means that the dynamic rupture increment at spontaneous failure is only associated with the external post-peak rupture energy $W_{r,ex}$. We can suppose that this is true for Class II rocks also, i.e.

Fig. 9 Variation of the dynamic increment of post-peak rupture energy $\Delta W_{r(d)}$ versus brittleness index K_1



$W_{r.in}$ is the same for the static failure regime and for dynamic spontaneous failure. This result is important because it is impossible to determine the post-peak rupture energy for Class II rocks at spontaneous failure. In the static regime the external deformation is negative, as a result of the specimen unloading (see Fig. 3). However, at spontaneous failure, the loading surfaces contacting the specimen ends will cause positive external deformation, contracting the specimen, thus preventing the measurement of the rupture energy.

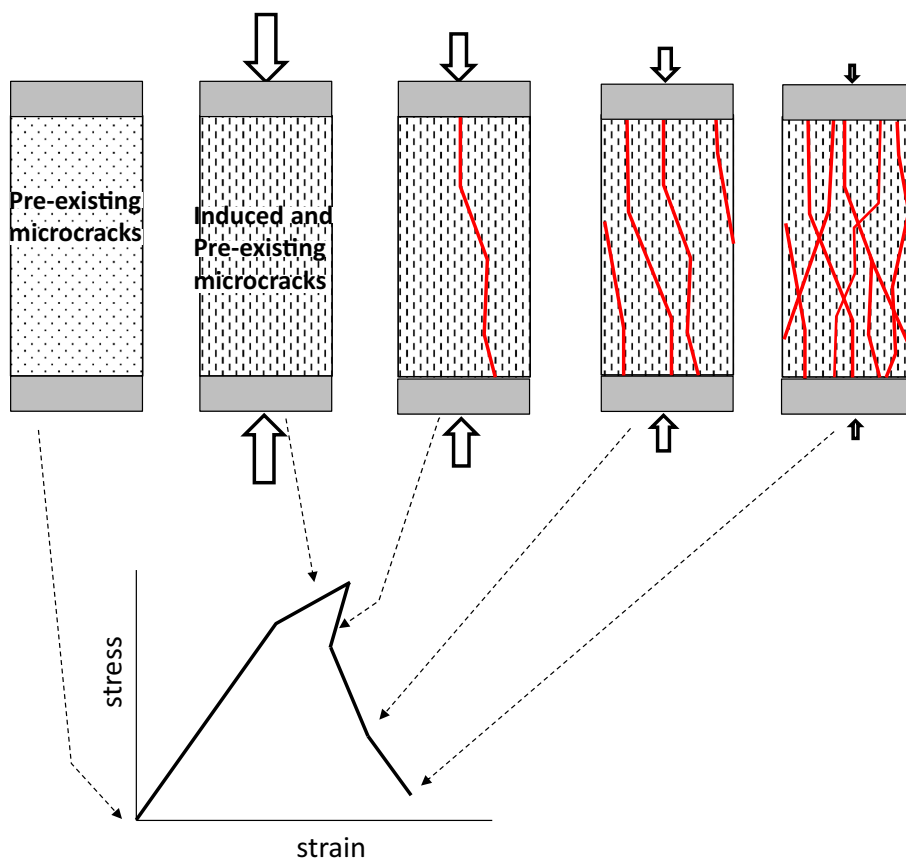
4.3 Compressive-Force Fragmentation Mechanism

Figure 10 illustrates schematically the failure and fragmentation mechanism acting in the majority of Class I and Class II rocks under uniaxial compression. According to this mechanism, loading of the material induces the creation and accumulation of microcracks, randomly distributed in the material body (e.g. Lockner et al. 1992). The microcracks are often generated at grain boundaries, representing the weakest elements of the microstructure. The macroscopic failure is associated with coalescence of the induced and pre-existing microcracks. The prevailing mode of macroscopic fracturing under uniaxial compression is the formation of extension fractures oriented

approximately in the direction of the major stress (red lines in Fig. 10). Decrease in bearing capacity of the material beyond the peak stress is normally associated with the stage of crack coalescence. Arrows in Fig. 10 indicate decreasing external forces applied by the loading system in accordance with the decreasing bearing capacity of the material at different stages of post-peak failure. Rock volumes totally surrounded by fractures or free surfaces form fragments. For the failure and fragmentation processes, the presence of external compressive forces is necessary. We will call this mechanism the ‘compressive-force’ fragmentation mechanism CFFM.

The degree of fragmentation is determined by how uniform and intensive the defect coalescence process is. The process of fracturing, and friction between rock fragments for Class I rocks, absorbs totally the elastic energy stored in the material at the peak stress, and, in addition, some elastic energy delivered from the loading system. At spontaneous failure the post-peak rupture energy $W_{r(d)}$ is different from the static post-peak rupture energy $W_{r(s)}$, which should affect the degree of fragmentation. The experiments presented in Fig. 6 show that variation of $W_{r(d)}$ and, consequently, variation in degree of fragmentation, takes place within a certain range of relatively high levels of loading stiffness only. Starting from a specific level of

Fig. 10 Compressive-force fragmentation mechanism



stiffness, both $W_{r(d)}$ and degree of fragmentation become independent of the loading stiffness. At high stiffness of the loading system, the failure violence can be mitigated by the increased energy consumption taking place at dynamic failure. At low stiffness of the loading system, this effect ceases due to independence of $W_{r(d)}$ from the loading stiffness.

5 Class II Rocks, Shock-Wave Fragmentation Mechanism as a Characteristic of Extreme Class II Behaviour, Energy Balance

5.1 Features of Post-peak Failure of Class II Rocks

Figure 11 shows stress-axial-lateral strain curves for Class II rocks tested in uniaxial compression: (a) granite (Jacobsson 2007) and (b) quartzite-1 (the most brittle of three types of quartzite tested in the frame of this paper). Both specimens (granite and quartzite-1) were unloaded after the post-peak stage X marked on the graphs. The similarity in behaviour of these two rocks lies in the fact that the magnitude of the post-peak modulus is very close to the magnitude of the pre-peak elastic modulus, indicating high

brittleness close to absolute brittleness on the scale in Fig. 2. A very important difference in behaviour of these two rocks is the fact that granite showed significant irreversible strain $\Delta\varepsilon$ before the peak stress, both in the axial and in the lateral directions, while the quartzite-1 showed this only in the lateral direction, with the axial irreversible strain close to zero $\Delta\varepsilon_1 \approx 0$. This difference is explained by fundamentally different failure mechanisms generated in these rocks.

The pre-peak failure mechanism operating in granite is discussed in Fig. 10 and is typical for the majority of rocks. Before the peak stress, it is associated with generation of new induced microcracks, randomly distributed in the material body, and further propagation of widely spread pre-existing microcracks under loading. The intensive irreversible deformation on the microlevel leads to significant macroscopic irreversible strain both in axial and lateral directions at the pre-peak loading stage. Brittle failure of such rocks in the post-peak region, characterised by brittleness index K_1 close to zero, normally takes place at the beginning of the post-peak stage and is associated with formation of the first macroscopic extension (or slightly inclined shear) fracture. However, after completion of the first fracture shown in Fig. 11a, new macroscopic ruptures

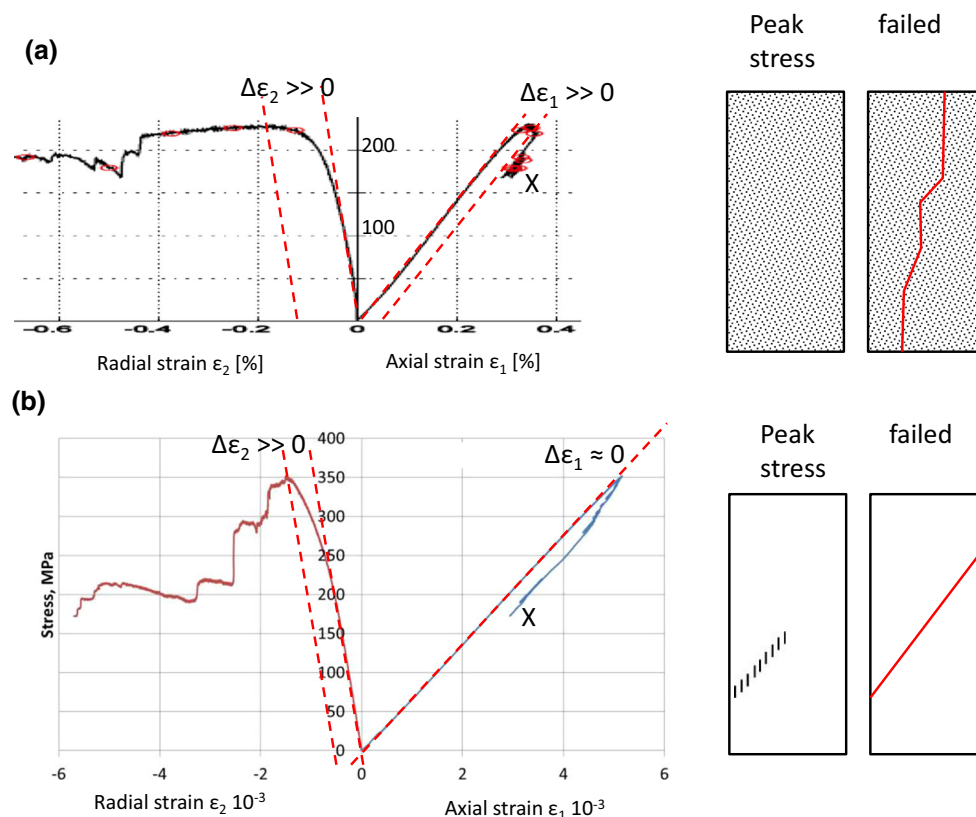


Fig. 11 Two failure mechanisms generated at uniaxial compression for Class II rocks illustrated by experimental results obtained on **a** granite and **b** quartzite-1

can be created, as shown in Fig. 10, which makes the post-peak modulus at this stage less steep, indicating a decrease in post-peak brittleness at this stage of failure.

In experiments on the quartzite-1, it was observed that the failure mode is a localised shear rupture. The reason for this is the specific microstructure of this quartzite. In general, quartzite is a metamorphic rock formed when quartz-rich sandstone or chert has been exposed to high temperatures and pressures. Such conditions fuse the quartz grains together forming a dense, hard, equigranular rock. Figure 12a (from Raith et al. 2012) illustrates features of quartzite microstructure when recrystallisation took place at different levels of pressure and temperature. The combination of high pressure and a temperature of about 700 °C (Stipp et al. 2002) causes grain boundary migration leading to creation of grain boundaries consisting of interfingering sutures (Fig. 12a-C). Studies of microstructure of quartzite-1 showed that it has this sort of microstructure, with grain boundaries consisting of interfingering sutures. In ‘normal’ rocks, grain boundaries represent the weakest elements of the structure, causing distributed microfracturing when loaded. With grain boundaries consisting of interfingering sutures, the grains are cemented together so firmly that when the rock fractures, the fractures pass through the grains not around them (Raith et al. 2012). This unique microstructure makes the quartzite-1 extremely strong (UCS is in the range 330–420 MPa) and brittle. Two other types of tested quartzite with ‘normal’ microstructure corresponding with

Fig. 12a-A, a-B exhibited significantly lower strength and brittleness: for quartzite-2, UCS is about 180 MPa and $K_1 \approx 0.8$; for quartzite-3, UCS is about 150 MPa and $K_1 \approx 1.15$.

Due to the very dense and quasi-homogeneous microstructure of quartzite-1, the ultimate failure mode of the quartzite-1 in uniaxial compression is the localised shear rupture consisting of a row of microtensile cracks. It is known that in brittle rocks a shear rupture propagates due to creation of microtensile cracks: the dilation of one short microcrack induces the dilation of closely spaced neighbouring cracks (Reches and Lockner 1994). Due to consecutive creation of short tensile cracks in front of the rupture tip, the advancing fault itself induces organised damage which is restricted to its own plane (see schematic representation of shear rupture in the specimen at peak stress in Fig. 11b). It is important to note that microcracks are generated along the major compressive stress which is at angle $\alpha_0 \approx (30^\circ\text{--}40^\circ)$ to the shear rupture plane (Reches and Lockner 1994; Horii and Nemat-Nasser 1985). This well-ordered microcracking process creates a row of intercrack slabs, known as domino-blocks. Each domino-block in the row in Fig. 11b is loaded elastically in the axial direction, which provides the absence (or negligibly small level) of irreversible axial strain observed for all tested quartzite-1 specimens. At the same time, vertically oriented microcracks separating the domino-blocks cause a significant pre-peak irreversible lateral strain. It should be noted that the development of localised shear rupture is not

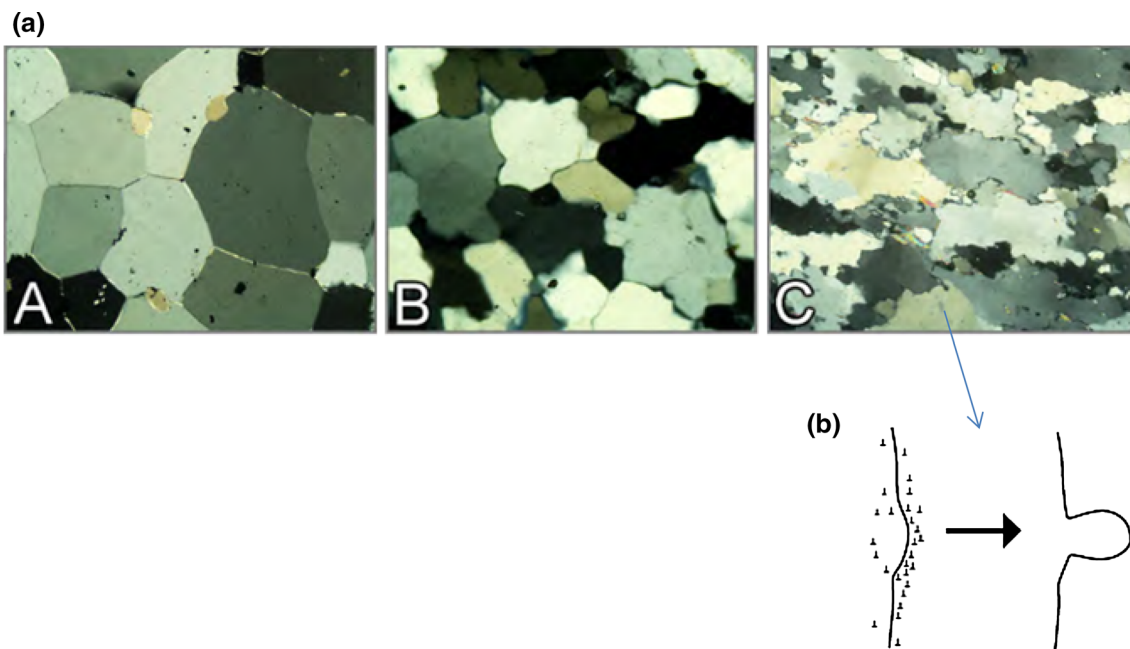


Fig. 12 **a** Microstructure of quartzite recrystallised at different levels of pressure and temperature. **b** Features of recrystallisation at high pressure and temperature (about 700 °C) associated with grain

boundary migration forming grain boundaries consisting of interfingering sutures (Raith et al. 2012)

accompanied by distributed microcracking typical for normal rocks. Thanks to this, the density of material outside the shear rupture stays practically at the initial high level.

It should be noted that in all tests on the quartzite-1, no complete post-peak curve could be obtained. Servo-control was based upon the feedback signal provided by lateral gauges. Controllable failure was very reliable at the initial post-peak stage associated with shear rupture development up to a critical length. After that, spontaneous and extremely violent failure took place, followed by very intensive rock fragmentation. The extended controllable post-peak rupture process was achieved only on one specimen, which contained a pre-existing healed shear plane (Fig. 11b). Despite the presence of the healed defect, this specimen showed the same strength and brittleness as other tested specimens and was unloaded before spontaneous failure occurred.

The impossibility of post-peak rupture control starting from a certain stage of the shear rupture development can be explained as follows. Figure 13 shows three stages of the shear rupture formation on the basis of localised microcracking forming a row of slabs (domino-like blocks). Observations show that in relatively soft rocks domino-blocks are subjected to rotation and collapse at shear displacement of the interfaces (Peng and Johnson 1972; King and Sammis 1992; Reches and Lockner 1994). However, it was proposed that in hard rocks with $UCS > 250$ MPa, due to the high strength of the domino-blocks, they can withstand rotation without collapse, operating as hinges (Tarasov 2014, 2016). Due to the consecutive creation and rotation of domino-blocks, they finally form a fan structure representing the shear rupture head (Fig. 13c). The fan structure has two extraordinary features: it decreases dramatically friction between shearing rupture faces and increases shear and tensile stresses in the rupture tip. The combination of these features provides

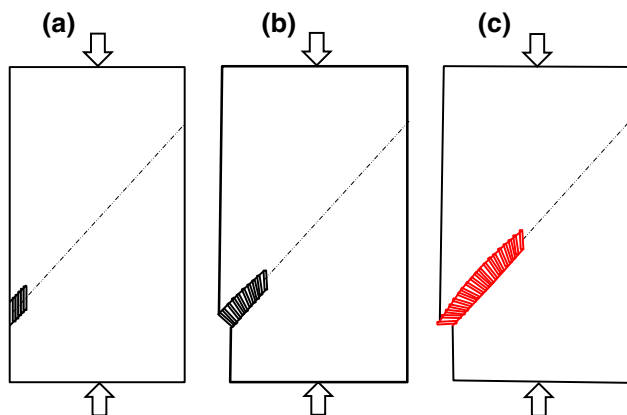


Fig. 13 Three stages of the fan structure formation at shear rupture development

conditions for shear rupture propagation with extreme dynamics. For the extreme rupture velocity, even very stiff and servo-controlled testing machines are not fast enough to prevent spontaneous failure by the specimen unloading.

Figure 14a shows stress–strain curves for four tested quartzite-1 specimens. Controllable failure associated with shear rupture development was provided until point A on the graphs after which spontaneous and explosive-like failure followed. All specimens exhibited post-peak modulus very close to the elastic modulus ($K_1 < 0.1$). Photographs in Fig. 14b show fragmented specimens after failure. They demonstrate that the degree of fragmentation is very sensitive to the level of compressive stress σ_A applied to the specimen at the moment at which instability starts. The specimen, which was unloaded before spontaneous failure, is divided by a shear rupture into two large pieces, with few small fragments. At spontaneous failure, specimen fragmentation is significantly greater, and the degree of fragmentation increases with increased compressive stress σ_A at which the instability started.

The behaviour of quartzite-1, as discussed above, is comparable with behaviour of bulk metallic glasses (BMG), which represent pronounced strong and brittle materials (Inoue et al. 2004; Zhang et al. 2006; Wu et al. 2008). BMGs have an amorphous structure with isotropic mechanical properties. It is observed that for BMG specimens subjected to uniaxial compression the initial stage of failure is associated with propagation of a shear rupture. Figure 15a shows a scanning electron micrograph image of a fragment of outer lateral surface of the bulk glass rod involving the shear rupture and unloaded before instability (Inoue et al. 2004). Initially, the shear rupture can propagate in the stable regime; however, when the rupture length reaches a critical length, catastrophic rupture propagation is followed, which is accompanied by a ‘bomb-blast-like’ sound and fragmentation into fine particles or powder. Figure 15b demonstrates the result of fragmentation taking place at the spontaneous failure regime (Wu et al. 2008).

5.2 Shock-Wave Fragmentation Mechanism as a Characteristic of Extreme Class II Behaviour

For BMG specimens, Inoue et al. (2004) explain the nearly simultaneous generation of a number of small fracture zones leading to fragmentation by a shock wave generated at an extremely high stress level. The shock wave can be generated due to the ‘instant’ shear rupture propagation forming rupture surfaces. The mechanism causing dramatic softening of shear rupture at the start of instability and catastrophic failure is unclear. Some results show that heat plays an important role in the softening (Yang et al. 2004). The fragmentation mechanism caused by shock waves has

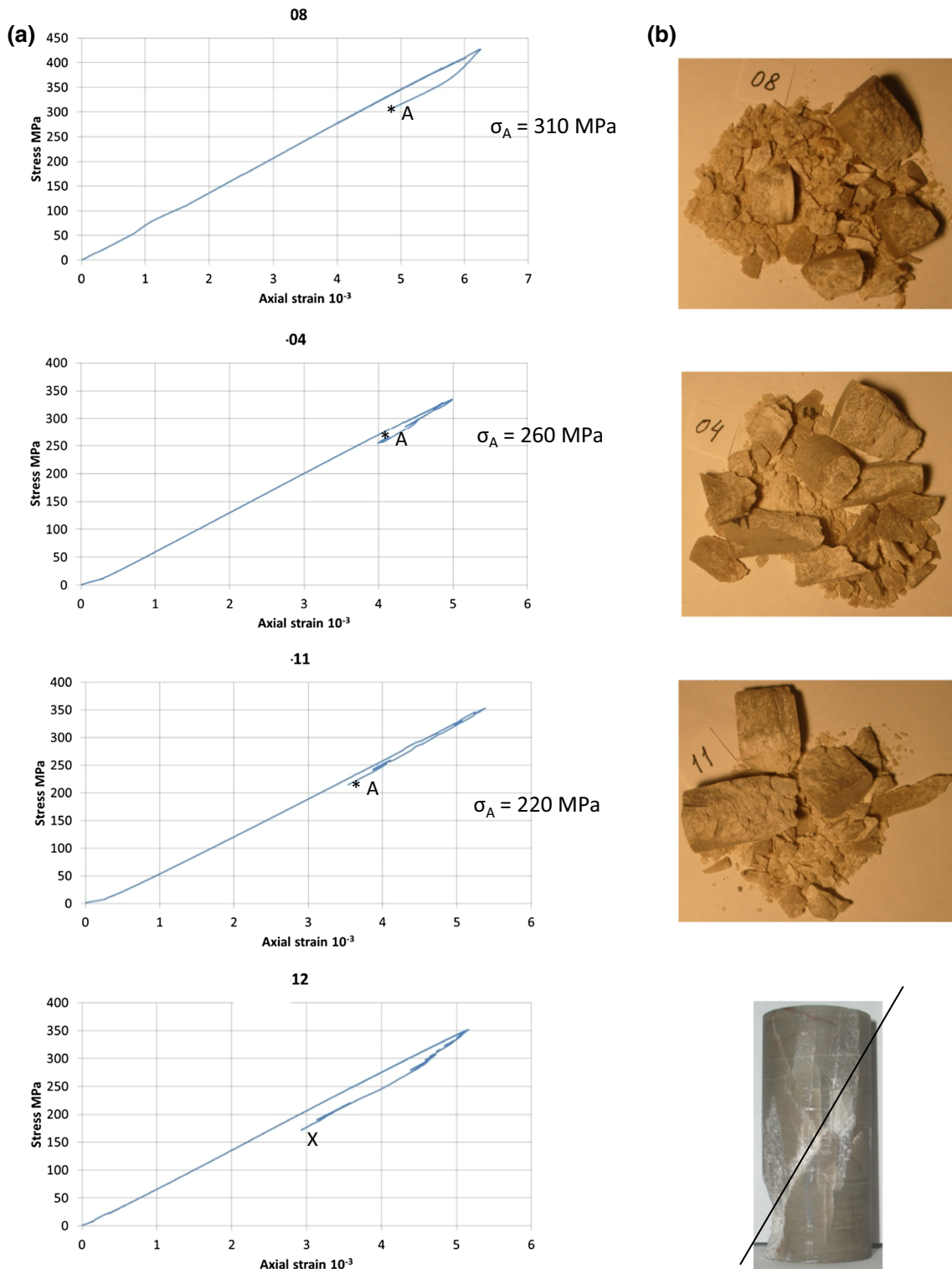


Fig. 14 a Stress–strain curves for quartzite-1 before instability; b photographs of the specimens after testing

been studied by many researchers (e.g. Galin and Cherepanov 1966; Grady 1981; Bless et al. 1992; Kanel et al. 2005). Galin and Cherepanov (1966), who observed an explosion-like fracture and fragmentation under bending of

high-strength glass, introduced a special term ‘failure wave’ characterising an important feature of the fragmentation mechanism. A hypothesis has been suggested that the fragmentation process takes place within a relatively

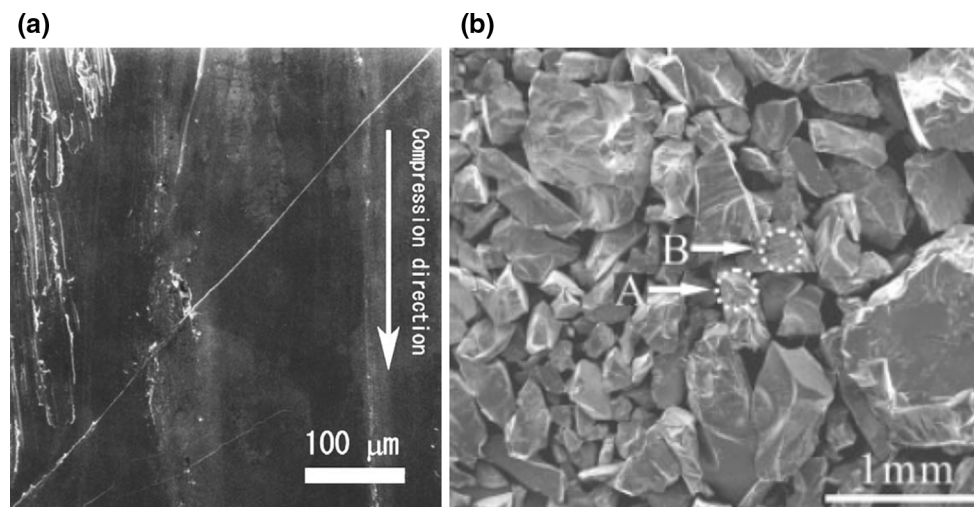


Fig. 15 Illustration of two failure mechanisms generated successively in metallic glasses at spontaneous failure under compression: **a** dynamic shear rupture propagation that is followed by **b** dramatic fragmentation

thin layer which propagates through undamaged material with high velocity. The fracture and fragmentation are caused by tensile stresses resulted from interaction of shock waves reflected from free surfaces. Within the propagating layer, the potential energy of the stressed body is transformed into new surfaces and kinetic energy of fragments. The failure waves can also be generated at impact loading. The important feature of failure waves is the fact that catastrophic fracture in elastically compressed media is not limited to impact events, but can continue after the external compressive forces have been ‘instantly’ released.

We suppose that the shock-wave mechanism is responsible also for fragmentation of quartzite-1 in uniaxial compression. To check how the potential elastic energy stored in the stressed body affects the degree of fragmentation, quartzite-1 specimens were tested additionally under dynamic loading. It is known that the dynamic fracture strength of rock can significantly exceed the static strength (e.g. Rinehart 1965; Stavrogin and Tarasov 2001). This means that the dynamic loading can ‘inflate’ larger compressive elastic energy into the specimen body. Figure 16a shows, schematically, features of the testing method used. A specimen was located in a steel protecting cylinder, the length of which was shorter by Δ than the specimen length (see stage I in Fig. 16a). The gap Δ is equal to axial dynamic deformation corresponding to the peak stress as illustrated schematically by the stress–displacement curve in Fig. 16b. In experiments the level of dynamic peak stress was about 600 MPa, which is significantly higher than the static strength (see Fig. 14a). After the peak stress, the specimen failure and fragmentation were caused by shock waves sourced by elastic energy stored in the specimen body. The higher amount of energy stored in dynamic

loading causes a significantly higher degree of material fragmentation compared with the static loading regime. Figure 16c shows that the whole specimen was fragmented into very small particles.

Hence, there are two fundamentally different fragmentation mechanisms which can be generated in brittle materials at uniaxial compression during spontaneous failure. The shock-wave mechanism can operate efficiently in brittle materials characterised by the following features: (1) material should be strong enough to accumulate a sufficient amount of potential elastic energy for generation of powerful shock waves; (2) material should be very dense to provide the propagation of elastic waves with minimum attenuation during numerous reflections and interactions; (3) material should provide extremely high velocity of the initial rupture propagation to generate the initial shock wave of great power. It is known that shear ruptures can propagate with significantly higher velocities compared with tensile ruptures and can approach the velocity of compressive elastic waves (Rosakis 2002). Hard rocks with the mentioned features can be classified as extreme Class II rocks. They can exhibit abnormal fragmentation and violence at spontaneous failure. We can expect that, on the scale of brittleness, the extreme Class II rocks should be characterised by a brittleness index K_1 very close to absolute brittleness. In less brittle rocks, the efficiency of the shock-wave fragmentation mechanism decreases; however, the compressive-force fragmentation mechanism becomes the prevailing mechanism. Figure 17 shows the universal scale of brittleness indicating positions of all three types of quartzite tested. Quartzite-1 exhibits extreme Class II behaviour, while quartzite-2 belongs to normal Class II and quartzite-3 showed Class I behaviour.

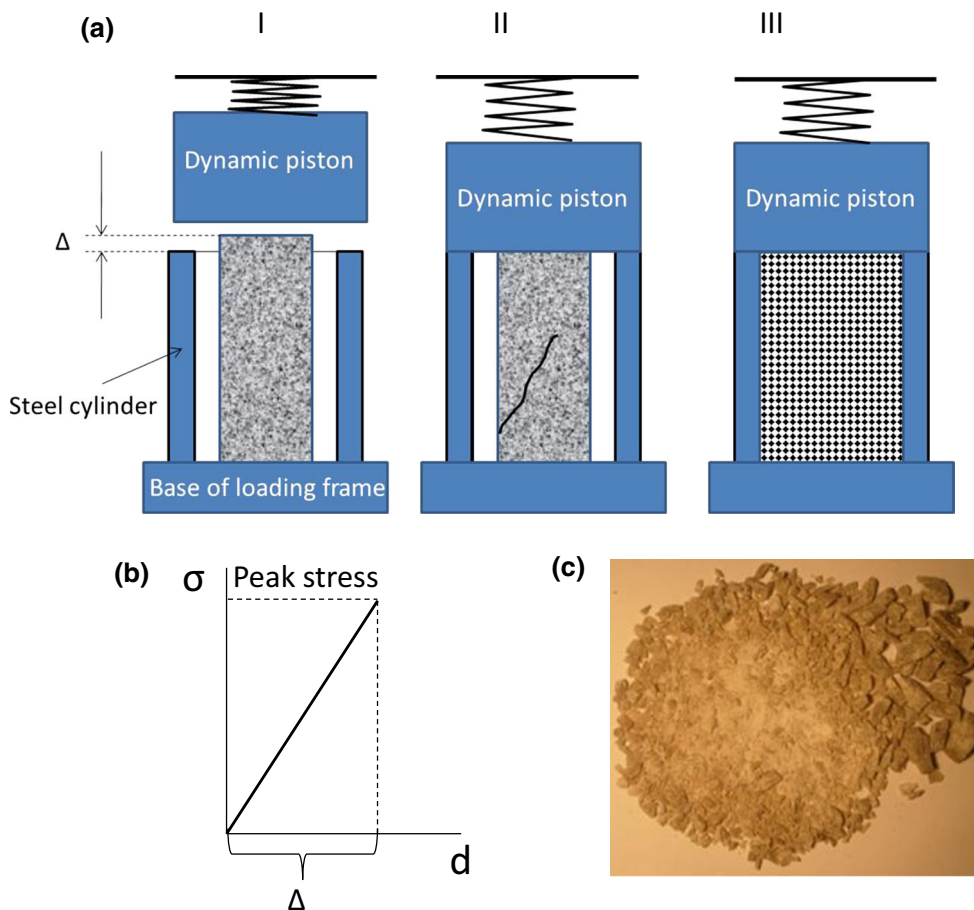
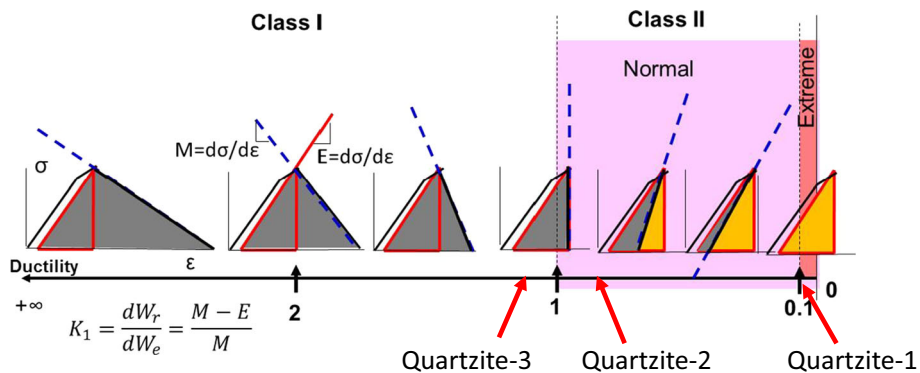


Fig. 16 a Schematic representation of the dynamic test conducted on the quartzite-1 specimen in the dynamic loading regime

Fig. 17 Universal scale of brittleness including normal and extreme Class II



5.3 Energy Balance of Class II at Spontaneous Failure

At the start of spontaneous failure, elastic energy is accumulated in the specimen body (W_e) and in the loading machine (W_H). First of all, we will discuss the role of these portions of energy in the fragmentation process. Due to the fact that quartzite-1 behaves as a glassy material, this question can be analysed on the basis of experimental

results obtained on glass specimens (Stavrogin 1968; Stavrogin and Tarasov 2001).

Experiments were conducted on tubular soda lime glass specimens (diameter 30 mm, thickness 1 mm, length 65 mm). The specimens were annealed at 500 °C before testing, to remove residual stresses. The specimens were loaded in a soft loading system to different levels of compressive stress, at which spontaneous failure was initiated, followed by fragmentation. The failure process was

triggered by a slight blow of a hard alloy bullet on the lateral surface of the glass tube or by other methods (eccentric specimen loading and local specimen heating). For all methods of triggering, results of fragmentation were comparable. After failure, the number of fragments was determined by sieve analysis. To understand the contribution of elastic energy stemming from the specimen, W_e , and from the loading system, W_H , to the fragmentation process, two different schemas of loading were used, as shown in Figs. 18a and 19a. In both cases, the loading stiffness was the same. Experimental results obtained for both loading schemas are shown in the graphs in Figs. 18b and 19b. They are presented with the following coordinates: horizontal axis—the specific elastic energy stored in the specimen before rupture initiation, $Q_e = W_e$; vertical axis—logarithm of the number of fragments, $\log n$.

In the first loading schema shown in Fig. 18a, the glass specimen was located between two large solid cylinders of the same acoustic impedance as the glass specimen. In this situation, the precisely prepared specimen–cylinder interfaces were transparent to the generated elastic shock stress waves, which allowed transfer from the specimen into the large volumes of the cylinders in which they were in contact. Thanks to this, the elastic energy, W_e , representing the source of shock stress waves, was removed from the specimen and practically excluded from the fragmentation process. The red line in Fig. 18b summarises experimental results (experimental points on the graph) obtained using this schema of loading. The results indicate that the degree

of fragmentation of the glass specimens for this testing condition was very small. In some of these experiments, specimens disintegrated into a few (sometimes into two) pieces. Figure 18c illustrates symbolically the character of fragmentation in this method of testing. The fragmentation observed in these tests was provided by the compressive-force fragmentation mechanism.

The second loading schema is shown in Fig. 19a. To minimise the chance of shock stress waves leaving the specimen, special acoustic boundaries were created between the specimen and the contacting loading cylinders. In some tests the boundaries were thin air chambers, as shown schematically in Fig. 19a. Due to the large differences in acoustic impedance between the glass and the boundaries, the stress waves sourced from the elastic energy, W_e , were trapped within the specimen. Shock stress waves are generated at spontaneous ‘instant’ failure of the highly compressed glass. Superposition of the initial shock waves and secondary waves, reflected from free surfaces, creates very large local tensile stresses, causing fragmentation. The extraordinary feature of this mechanism (in contrast with the compressive-force mechanism) is the creation of intensive fragmentation after the external forces initially applied to the material have vanished. The schematic representation of the fragmentation process is shown in Fig. 19c. Experimental results summarised by the red line in Fig. 19b show that the degree of fragmentation increases with the increase in amount of elastic energy, Q_e (or W_e), stored in the material at the moment of fracture

Fig. 18 Fragmentation of glass specimens for ‘transparent’ interfaces between the specimen and the loading system

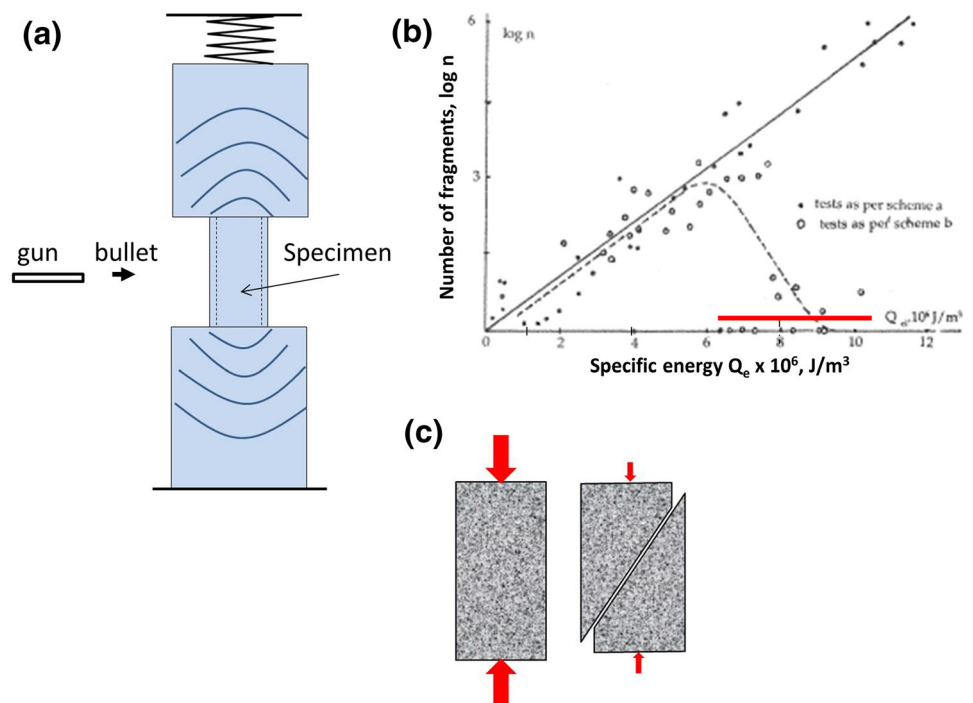


Fig. 19 Fragmentation of glass specimens at ‘opaque’ interfaces between the specimen and the loading system

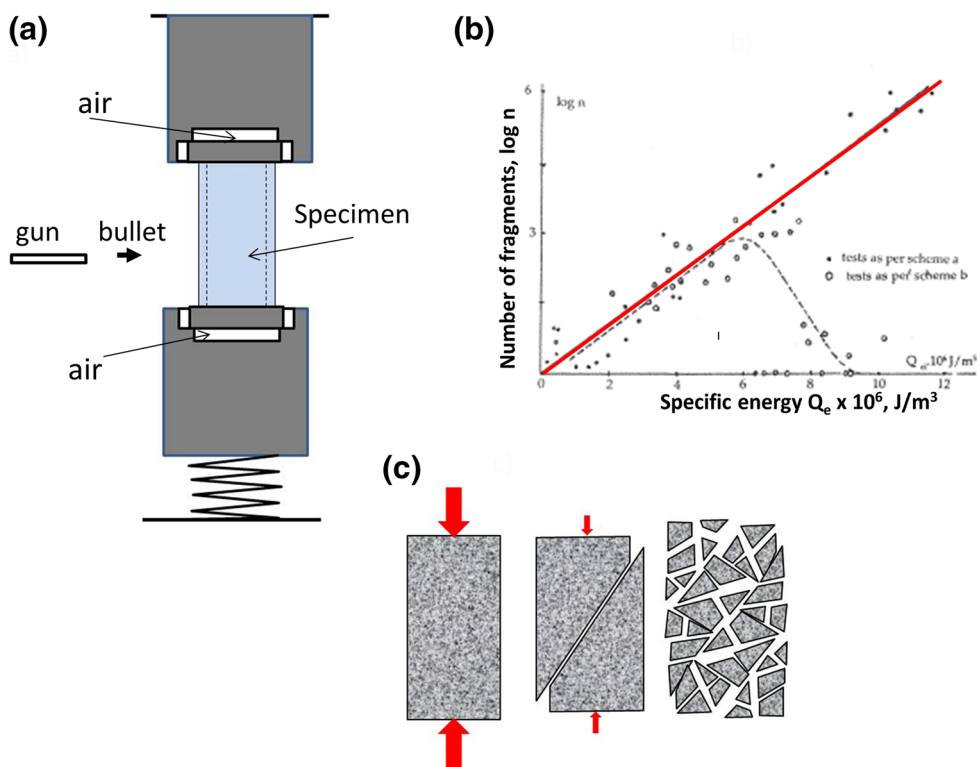
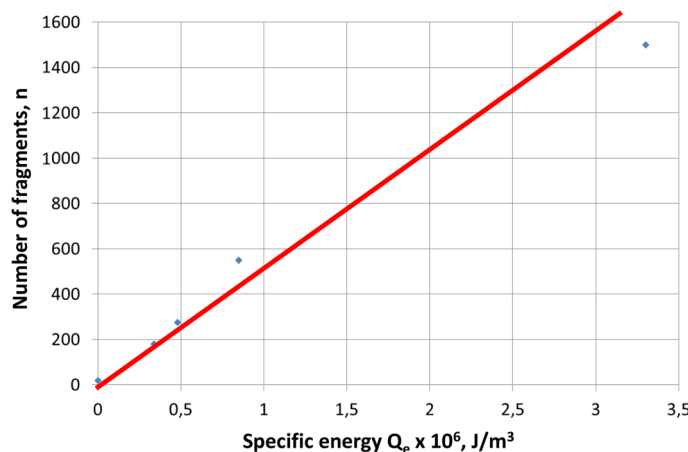


Fig. 20 Relation between the specific elastic energy Q_e stored in quartzite-1 specimens at the moment of spontaneous failure and the number of fragments n into which the specimens are fragmented



initiation. The maximum number of fragments is about a million.

The experiments described above have shown that the shock-wave fragmentation is sourced solely from elastic energy, W_e . The elastic energy, W_H , stemming from the loading system, is practically excluded from the fragmentation process. We can suppose that this is true for all extreme Class II materials. The graph in Fig. 20 summarises fragmentation results obtained in all tests on the

quartzite-1 (Figs. 14, 16). It shows the variation of the number of fragments, n , versus the amount of specific energy, Q_e . The quartzite-1 results show a linear relation between these parameters in contrast with the glass specimens where a logarithmic relation was observed. This difference can be explained by the fact that the material structure of quartzite-1 is less dense and homogeneous compared with glass. Furthermore, the maximum amount of energy stored in quartzite-1 is four times less than in

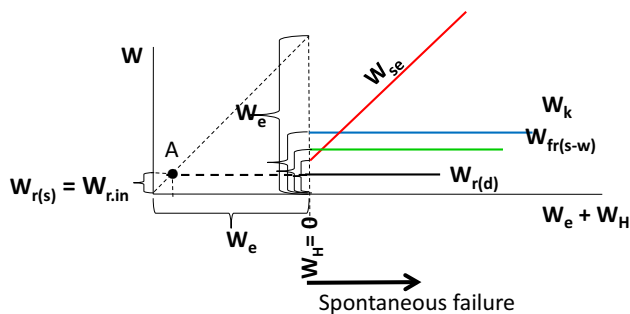


Fig. 21 Schematic representation of the total energy balance versus elastic energy stored in the specimen and loading system ($W_e + W_H$) for extreme Class II rocks

glass because of lower strength. Nevertheless, both materials demonstrate that the greater the amount of elastic energy stored in the specimen before the spontaneous failure, the greater the degree of fragmentation. We can conclude that at high levels of Q_e extreme Class II materials can exhibit dramatic fragmentation.

Schematic representation of the energy balance for extreme Class II rocks is shown in Fig. 21. The horizontal axis represents the elastic energy stored in the specimen, W_e , and in the loading system, W_H . The vertical axis characterises values of the different types of energy into which the elastic energy transforms at failure. Spontaneous failure can occur even at absolutely stiff loading conditions in which $W_H = 0$. In this case, the elastic energy stored in the specimen, W_e , transforms into: (1) rupture energy $W_{r(d)}$ associated with the formation of the first dynamic rupture, which ‘instantly’ realises the applied external forces; (2) fragmentation energy $W_{fr(s-w)}$ associated with the shock-wave fragmentation mechanism; (3) kinetic energy of fragments W_k ; and (4) seismic energy W_{se} associated with oscillation of the loading system caused by propagation of elastic waves. The relation between the magnitudes of these forms of energy can be very different, which requires special experimental studies. It is important to note that, for soft loading conditions, the elastic energy W_H is totally transformed into seismic energy W_{se} . The remaining components of energy should stay the same, because, at the ‘instant’ failure and fragmentation, the inertial loading system loses contacts with the specimen. Rockbursts associated with spontaneous failure of extreme Class II rock should be especially violent and accompanied by very large volumes of rock fragments ejected into the opening.

6 Conclusion

The paper discusses features of the energy balance at failure and fragmentation of Class I and Class II rocks. It demonstrates that the division of rocks into two classes (I and II) on the basis of post-peak modulus represents a rough characterisation on rock brittleness. A more detailed approach for rock brittleness characterisation within the range from absolute brittleness up to absolute plasticity used in the paper is based upon the ratio between the post-peak rupture energy dW_r and the elastic energy dW_e released at failure: $K_1 = dW_r/dW_e$. According to this approach, Class I rocks are characterised by $\infty > K_1 > 1$ while Class II rocks are characterised by $1 > K_1 > 0$.

The paper analyses features of the energy balance at spontaneous failure of specimens on the basis of experimental results obtained for rocks with brittleness index within the range $6 \geq K_1 > 0$ and wide variation of the loading stiffness. It is shown that elastic energy stemming from the loading system W_H is responsible for dynamic post-peak failure for Class I rocks only. It sources the dynamic rupture process and increases post-peak rupture energy. Moreover, the less brittle the rock, the greater the dynamic increment of the rupture energy. This rupture energy increment creates a damping effect by absorbing a portion of energy W_H which decreases the failure violence. For Class II rocks, the failure process is sourced solely by elastic energy stemming from the specimen W_e . The energy W_H transforms totally into seismic energy.

The paper specifies the most brittle Class II rocks as extreme Class II. For such rocks, the intensive fragmentation process is provided by a shock-wave fragmentation mechanism. This mechanism is associated with interaction of reflected tensile shock stresses generated in the material body due to the ‘instant’ release of external forces caused by dynamic fracturing. The fragmentation process caused by external forces is referred to in the paper as the compressive-force fragmentation mechanism.

Acknowledgements The authors acknowledge the support provided by the Centre for Offshore Foundation Systems (COFS) at the University of Western Australia.

Appendix

See Fig. 22.

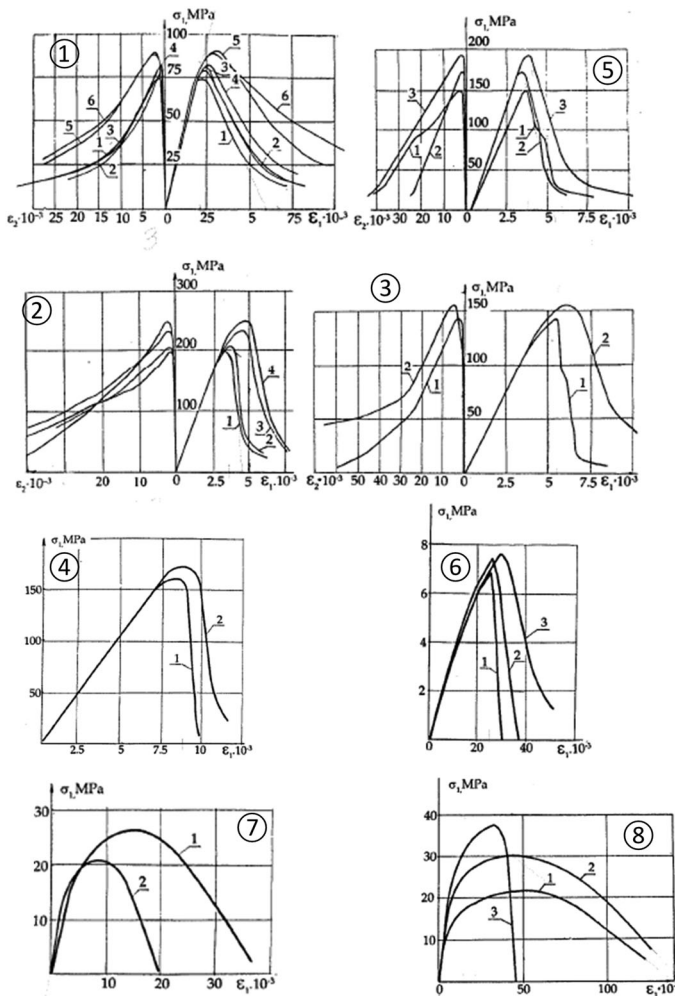


Fig. 22 Stress–strain curves obtained at different strain rates for 1 marble, 2 granite, 3 sandstone-1, 4 sandstone-2, 5 sulphide ore, 6 lignite, 7 rock salt, 8 sylvinitite. During each test constant, strain rate

Table

①	marble					
	Curve no.	1	2	3	4	5
	$\dot{\epsilon}_1$ s ⁻¹	2×10^{-6}	2×10^{-5}	2×10^{-4}	2×10^{-3}	2×10^{-2}
⑤	sulphide ore					
	Curve no.	1	2	3		
	$\dot{\epsilon}_1$ s ⁻¹	10^{-5}	5×10^{-2}	2×10^{-1}		
②	granite					
	Curve no.	1	2	3	4	
	$\dot{\epsilon}_1$ s ⁻¹	10^{-5}	2×10^{-4}	5×10^{-2}	2×10^{-1}	
③	NBP sandstone					
	Curve no.	1	2			
	$\dot{\epsilon}_1$ s ⁻¹	3×10^{-6}	10^{-1}			
④	BP sandstone					
	Curve no.	1	2			
	$\dot{\epsilon}_1$ s ⁻¹	10^{-5}	2×10^{-1}			
⑦	rock salt					
	Curve no.	1	2			
	$\dot{\epsilon}_1$ s ⁻¹	2×10^{-5}	2.5×10^0			
⑥	lignite					
	Curve no.	1	2	3		
	$\dot{\epsilon}_1$ s ⁻²	10^{-4}	10^{-2}	10^0		
⑧	sylvinitite					
	Curve no.	1	2	3		
	$\dot{\epsilon}_1$ s ⁻¹	10^{-8}	10^{-6}	4×10^0		

References

Andreev GE (1995) Brittle failure of rock materials. Balkema, Rotterdam

Aubertin M, Gill DE, Simon R (1994) On the use of the brittleness index modified (BIM) to estimate the post-peak behaviour of rocks. In: Proceedings of the 1st North American rock mechanics symposium, Balkema, pp 945–952

Bergman SGA, Stille H (1983) Rockburst problems in a 2.6 million m³ underground crude oil storage in granite. In: Proceedings of the fifth congress ISRM, pp D302–D309

Bieniawski ZT (1970) Time-dependent behaviour of fractured rock. Rock Mech 2:123–137

Bless SJ, Brar NS, Kanel G, Rosenberg Z (1992) Failure waves in glass. J Am Ceram Soc 75(4):1002–1004

Clucklich J, Cohen LJ (1967) Size as a factor in the brittle–ductile transition and the strength of some materials. Int J Fract Mech 3:278–289

Coates DF (1966) Experimental criteria for classification of rock substances. Int J Rock Mech Min Sci 3:181–189

Cook NGW (1965) The failure of rock. Int J Rock Mech Min Sci 2:389–403

was provided before and after peak stress. The magnitude of strain rate $\dot{\epsilon}_1$ for each stress–strain curve is presented in the table (from Stavrogin and Tarasov 2001)

Dight PM, Tarasov BG, O’Hare AW (2013) Determining the proneness of rock to strainburst. In: Malovichko, A, Malovichko, D (eds) 8th international symposium on rockbursts and seismicity in mines. ISBN: 978-5-903258-28-4

Drescher A, Vardoulakis I (1982) Geometric softening in triaxial tests on granular material. Geotechnique 32:291–3003

Galin LA, Cherepanov GI (1966) On self-supporting failure of a stressed brittle solid. Dokl AN SSSR 167(3):543–546 (in Russian)

Grady DE (1981) Fragmentation of solids under impulsive stress loading. J Geophys Res 86(B2):1047–1054

He C, Okubo A, Nishimatsu Y (1990) A study on the class II behaviour of rock. Rock Mech Rock Eng 32:261–273

Horii H, Nemat-Nasser S (1985) Compression-induced micro-crack growth in brittle solids: axial splitting and shear failure. J Geophys Res 90:3105–3125

Hucka V, Das B (1974) Brittleness determination of rocks by different methods. Int J Rock Mech Min Sci 11:389–392

Hudson JA, Crouch SL, Fairhurst C (1972) Soft, stiff and servo-controlled testing machines: a review with reference to rock failure. Eng Geol 6:155–189

- Inoue A, Shen BL, Chang CT (2004) Super-high strength of over 4000 MPa for Fe-based bulk glassy alloys. *Acta Mater* 52:4093–4099
- Jacobsson L (2007) Forsmark site investigation—Borehole KFM01C—UCS. SP Swedish National Testing and Research Institute, Boras
- Kaiser PK, Cai M (2013) Critical review of design principles for rock support in burst-prone ground-time to rethink!. In: Potvin Y, Brady B (eds) Proceedings of the seventh international symposium on ground support in mining and underground construction, Australian Centre for Geomechanics, Perth, pp 3–37
- Kanel GI, Razorenov SV, Fortov VE (2005) A failure wave phenomenon in brittle materials. In: Joint 20th AIRAPT–43th EHPRG, Karlsruhe/Germany
- Kidybinski A (1981) Bursting liability indices of coal. *Int J Rock Mech Min Sci* 18:295–304
- King GCP, Sammis CG (1992) The mechanisms of finite brittle strain. *PAGEOPH* 138(4):611–640
- Labuz JF, Biolzi L (1991) Class I vs Class II stability: a demonstration of size effect. *Int J Rock Mech Min Sci Geomech Abstr* 28(2/3):199–205
- Lockner DA, Byerlee JD, Kuksenko V, Ponomarev A, Sidorin A (1992) Observations of quasi-static fault growth from acoustic emissions. In: Evans B, Wong T-F (eds) Fault mechanics and transport properties of rocks. Academic, San Diego, pp 3–31
- McGarr A (1997) A mechanism for high wall-rock velocities in rockbursts. *Pure appl Geophys* 150:381–391
- Okubo S, Nishimatsu Y, He C (1990) Loading rate dependence of Class II rock behaviour in uniaxial and triaxial compression tests—an application of a proposed new control method. *Int J Rock Mech Min Sci Geomech Abstr* 27(6):559–562
- Ortlepp WD, Stacey TR (1994) Rockburst mechanisms in tunnels and shafts. *Tunn Undergr Space Technol* 9(1):59–65
- Peng S, Johnson AM (1972) Crack growth and faulting in cylindrical specimens of Chelmsford granite. *Int J Rock Mech Min Sci* 9:37–86
- Petoukhov IM, Linkov AM (1983) Mechanics of rockburst and outburst. Nedra, Moscow
- Raith MM, Raase P, Reinhardt J (2012) Guide to thin section microscopy, 2nd edn. ISBN: 978-3-00-037671-9
- Read HE, Hegemier GA (1984) Strain softening of rock, soil and concrete—a review article. *Mech Mater* 3:271–294
- Reches Z, Lockner DA (1994) Nucleation and growth of faults in brittle rocks. *J Geophys Res* 99(B9):18159–18173
- Rinehart JS (1965) Dynamic fracture strengths of rocks. In: Proceedings of the seventh symposium on rock mechanics. Pennsylvania State University
- Rosakis AJ (2002) Intersonic shear cracks and fault ruptures. *Adv Phys* 51(4):1189–1257
- Stavrogin AN (1968) Strength and deformation of rocks. Highest doctoral degree of technical science. The USSR State Geomechanical Institute, Leningrad
- Stavrogin AN, Protossenia AG (1985) Rock strength and excavation stability in great depth. Nedra, Moscow
- Stavrogin AN, Tarasov BG (2001) Experimental physics and rock mechanics. Balkema, Rotterdam
- Stipp M, Stunitz H, Heilbronner R, Schmid SM (2002) The eastern Tonale fault zone: a ‘natural laboratory’ for crystal plastic deformation of quartz over a temperature range from 250 to 700°C. *J Struct Geol* 24:1861–1884
- Tarasov BG (2010) Superbrittleness of rocks at high confining pressure. Keynote lecture In: Van Sint Jan M, Potvin Y (eds) Fifth international seminar on deep and high stress mining, Santiago, Chile, pp 119–133
- Tarasov BG (2014) Hitherto unknown shear rupture mechanism as a source of instability in intact hard rocks at highly confined compression. *Tectonophysics* 621:69–84
- Tarasov BG, Potvin Y (2013) Universal criteria for rock brittleness estimation under triaxial compression. *Int J Rock Mech Min Sci* 59:57–69
- Wawersik WR, Fairhurst C (1970) A study of brittle rock fracture in laboratory compression experiments. *Int J Rock Mech Min Sci* 7:561–575
- Wu FF, Zhang ZZ, Shen BL, Mao SXY, Eckert J (2008) Size effect on shear fracture and fragmentation of a bulk metallic glass. *Adv Eng Mater* 10(8):727–730
- Xu YH, Cai M (2017) Influence of loading system stiffness on post-peak stress-strain curve of stable rock failures. *Rock Mech Rock Eng*. doi:10.1007/s00603-017-1231-1
- Yang B, Liaw PK, Wang G, Morrison M, Liu CT, Buchanan RA, Yokoyama Y (2004) In-situ thermographic observation of mechanical damage in bulk-metallic glasses during fatigue and tensile experiments. *Intermetallics* 12:1265–1274
- Zhang ZF, Zhang H, Shen BL, Inoue A, Eckert J (2006) Shear fracture and fragmentation mechanisms of bulk metallic glasses. *Philos Mag Lett* 86(10):643–650